BUTTERWORTH HEINEMANN

Buoyancy effects on the mass transfer in absorption with a nonabsorbable gas

J. Chen and K. E. Herold
Department of Mechanical Engineering, University of Maryland at College Park, College Park, MD, USA

This paper describes the vapor side buoyancy effects on the mass transfer in absorption in the presence of a nonabsorbable gas. Experimental results on a diffusion–absorption refrigerator (DAR) indicate that the vapor side buoyancy effects on the mass transfer are significant when the density of the nonabsorbable gas is significantly less than that of the absorbable gas. A rectangular enclosure absorption problem is first solved to demonstrate the buoyancy effects without the presence of a forced flow. Then, mixed convection heat transfer in a circular pipe is simulated in such a way as to be analogous to the mixed convection mass-transfer problem in the DAR absorber. Finally, the vapor side mixed convection absorption between parallel plates is simulated including the effects of the absorbed mass on the mass balance. The Sherwood number dependence on the mass transfer Grashof number and Reynolds number as well as the effects of the suction boundary conditions are discussed. Each of these simulations had individual limitations, but, taken together, they illuminate the major aspects of the absorption physics.

Introduction

The absorption of gases and vapors in liquid is encountered in numerous engineering applications. In many cases of interest, such as the absorption of water vapor into concentrated brine, the resistance to absorption in the vapor phase is negligible. However, in the presence of a nonabsorbable gas in the vapor phase, the mass transfer resistance on the vapor side can be of significant importance. One such application can be found in the absorption process of diffusion–absorption refrigerators (DAR) (Kim et al. 1993).

The absorption process in the DAR is shown schematically in Figure 1. A forced stream of ammonia-hydrogen (or helium) vapor mixture enters the lower section of a slightly inclined circular pipe (absorber). It flows up in counterflow against an ammonia–water liquid film falling down along the bottom of the absorber. During the absorption process, the inlet ammonia mass fraction of liquid and vapor mixtures are typically 0.12 and 0.65, respectively. The total pressure in the system is 25 bar, and the temperatures along the absorber are from 35 to 55°C. Under such operating conditions, the inlet ammonia partial pressure of the vapor mixture is significantly higher than the inlet ammonia vapor pressure at the liquid–vapor interface. Thus, absorption of ammonia takes place accompanied by energy release at the interface. This absorption process results in a mass fraction gradient in the vapor phase due to the presence of the nonabsorbable gas (hydrogen). The diffusion of ammonia from the bulk vapor flow to the interface would slow down the absorption process considerably if there were no gravitational field. Fortunately, the vapor mixture at the interface becomes lighter as ammonia is absorbed into the liquid, because hydrogen is significantly lighter than ammonia. The existence of the buoyancy force causes buoyancy-induced convection to occur and enhances the heat and mass transfer. This mixed-convection process is characterized by considerable complexity and sensitivity to changes in the boundary conditions.

Diffusion–absorption refrigeration test results exhibit characteristics consistent with buoyancy-induced flow. Table 1 gives the absorber inlet and outlet conditions during a typical run with a hydrogen charge.

In Table 1, the density stands for the density of the vapor mixture, and the mass concentration of ammonia stands for the mass of ammonia per unit volume. Based on assumed linear mass fraction profiles between vapor inlet and outlet, the averages of the inlet and the outlet ammonia mass concentration at the interface ρ_{Ai} and bulk stream ρ_{Am} can be used to estimate the absorption rate using the following equation.

$$m_A = h_m A(\rho_{Am} - \rho_{Ai}) \tag{1}$$

In Equation 1, the mass transfer coefficient is calculated using a diffusion model (Incropera and DeWitt 1990; Shi 1994). The value used for the results presented here is $h_m = 0.00122$ m/s. The liquid–vapor interface area ($A = 0.024$ m^2) is estimated as follows: (1) The laminar falling film theory is used to determine the mass flow rate of the absorbent film as a function of film thickness and width; (2) this relation is then used along with the geometry of the absorber to estimate the film width for a given flow rate; and (3) the interface area is calculated knowing the width of the liquid film and the total length of the absorber (Shi). The absorption rate of ammonia obtained using Equation 1 was found to be 0.0299 g/s. However, our experimental data (Kim et al. 1994) show an absorption rate of 0.053 g/s, which indicates the possible significance of buoyancy effects. Experiment results also show that the absorber capacity of a DAR charged with helium is about 17% lower than when charged with hydrogen (Kim et al.). Hydrogen and helium have similar diffusion coeffi-

Address reprints requests to Mr. Jie Chen, Appliance Technology Center, Amana Refrigeration, Inc., Amana, IA 52204, USA.

Received 12 March 1995; accepted 23 August 1995

Int. J. Heat and Fluid Flow 16: 536–545, 1995
© 1995 by Elsevier Science Inc.
655 Avenue of the Americas, New York, NY 10010

0142-727X/95/$10.00
SSDI 0142-727X(95)00074-7

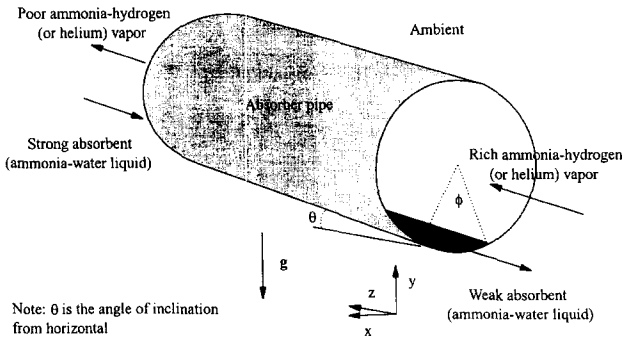

Figure 1 Absorption in diffusion–absorption refrigeration absorber

cients; whereas, the density of the ammonia–helium mixture is 83% higher than that of the ammonia–hydrogen mixture under typical absorption conditions in the DAR (pressure = 25 bar, temperature = 40°C, and mass fraction of ammonia = 45%). Buoyancy effects can explain the inferior absorber performance observed with helium.

A review of the present state of knowledge in film absorption was conducted by Grossman (1991). He points out several factors that influence the absorption process. These are: (1) the physical properties of the fluids; (2) the flow regime — laminar, wavy, or turbulent; (3) the thermodynamic equilibrium properties of the participating substances; (4) local instabilities and secondary flows at the interface due to surface tension gradients, surface impurities, and buoyant forces; and (5) the heat transfer at the solid wall. Grossman (1983) made both theoretical and numerical analyses on the absorption of water vapor on a brine film absorption with constant temperature and adiabatic wall boundary conditions. Grossman (1983, 1990) also studied the effects of nonabsorbable gases and interdiffusion. Brauner et al. (1989) performed a similar analysis except that all the convective terms in the diffusion equations and variation of film thickness were considered. Yih and Seagrave (1980) studied the effects of interfacial shear on the mass transfer rate. Rashidi et al. (1975) studied the mechanism of heat and mass transport at gas–liquid interfaces based on their experiments. The study of transfer enhancement by surfactant additives were made by Kashiwagi (1985), Burnett and Himmelblau (1970), and many other researchers. During the literature search, no reference has been found that considers buoyancy effects on the rate of absorption.

Buoyancy effects have significant importance in many engineering applications. In certain cases, such as film condensation in the presence of noncondensable gas, solar ponds, and combustion studies, the density gradients in the system are important and have been extensively studied. However, these processes distin-

Notation

A	area of liquid–vapor interface, m^2
b	width of the two parallel plates or width of the rectangular enclosure, m
D	binary diffusion coefficient, m^2/s
g	gravitational acceleration, m/s^2
Gr	Grashof number $[gh^3\beta(t_b - T_i)]/\nu^2$
Gr_m	mass transfer Grashof number, $[gh^3\zeta(\rho_{B2} - \rho_{B1})]/\nu^2$
h	height of the rectangular enclosure or distance between the parallel plates, m
h_m	mass transfer coefficient, m/s
h_T	heat transfer coefficient, $W/m^2 \cdot K$
I	mesh size in x or X directions
J	mesh size in y or Y directions
K	mesh size in z or Z directions
k	thermal conductivity $W/m \cdot K$
m	absorption rate, kg/s
n	mass flux, $kg/m^2 \cdot s$
Nu	Nusselt number, $h_T h/k$
p	pressure, kPa
P	dimensionless pressure
Pr	Prandtl number, ν/α
q	heat flux, kW/m^2
r	radius of the pipe, m
Ra	Rayleigh number, GrPr
Ra_m	mass transfer Rayleigh number, $Gr_m Sc$
Re	Reynolds number, hu_m/ν
RES	normalized residue (residue at any iteration divided by residue at first iteration)
Sc	Schmidt number, ν/D
Sh	Sherwood number, $h_m h/D$
T	temperature (°C or K)
T_{avg}	average temperature, K
T_{wall}	wall temperature, K
u, v, w	x, y, and z direction velocity, respectively, m/s
u_c	characteristic velocity, m/s
u_{max}	maximum velocity at the vapor inlet, m/s
U, V,	X, Y (dimensionless) direction velocity, respectively
x_A, x_B	mass fraction of component A and B, respectively
x_{Bm}	mean mass fraction of component B at a given cross section
x, y, z	coordinates, m
x_A, x_B	dimensionless mass fraction of component A and B, respectively
X, Y,	nondimensional coordinates

Greek

α	thermal diffusivity, m/s^2
ζ	species expansion coefficient, defined in Equation 18, m^3/kg
θ	angle between the centerline of the circular pipe (or the parallel plates) and the horizontal plane, radians or °
μ	dynamic viscosity, $N \cdot s/m^2$
ν	kinematic viscosity m^2 s
ρ	density, kg/m^3
ρ_{Ai}	average vapor mass concentration at the liquid–vapor interface, kg/m^3
ρ_{Am}	average vapor mass concentration of ammonia of bulk stream, kg/m^3
ϕ	angle of wetted liquid film in the circular pipe, radians or °

Subscripts

1	top, inlet
2	bottom
A	absorbable gas, ammonia
B	nonabsorbable gas
m	mean, bulk, or mass transfer
x, y,	coordinates

guish themselves from the absorption process by physical phenomena as well as geometric configurations. Most research has been done on the buoyancy effects attributable to density gradients resulting from inhomogeneities in temperature. In many cases, those results can be used to evaluate quantitatively the buoyancy effects attributable to density differences resulting from inhomogeneities in species concentration by applying heat and mass transfer analogies.

Mixed convection in horizontal tubes has been the subject of continuing investigation since the pioneering work by Graetz in 1885 (Gebhart et al. 1988). Many different boundary conditions and flow regimes have been investigated (Gebhart et al.). Among those studies, the work by Patankar et al. (1978) seems most relevant to the present study. They carried out a computational study of the fully developed laminar flow and heat transfer in a horizontal tube that is subject to nonuniform circumferential heating. In the case of top half insulated and bottom half uniformly heated, a Nusselt number augmentation of ten times was reported at large Grashof number due to buoyancy effects. In this case, the buoyancy forces generate a secondary helical flow pattern superimposed on the main flow. For a straight tube, this motion is a pair of helical circulations. The experimental visualization of this secondary flow was reported earlier by Mori and Futagami (1967). Based on the heat and mass transfer analogy, a similar phenomenon is expected in the DAR absorber driven by concentration density gradients.

Mixed convection in noncircular channels was studied by Cheng et al. (1972), Ou et al. (1974), and several other researchers. The results are quite similar to those in circular tubes (Gebhart et al. 1988). Mixed convection between two wide parallel surfaces has received less attention than those in tubes and channels. In the case of horizontal flows, deformation of the otherwise symmetric velocity profile due to buoyancy effects was reported. The maximum velocity occurs above or below the center plane, depending on whether the fluid is being cooled or heated as it flows between the surfaces (Gebhart et al.). Kennedy and Zebib (1982) made both experimental and numerical investigations on the mixed convection between horizontal parallel plates with a line heat source on the bottom plate. A recirculating flow region was found superimposed on the main flow at the location of the heat source. Near the heat source, heat transfer enhancement of about a factor of two was reported.

The objective of the present investigation is to quantify the vapor side buoyancy effects on the rate of absorption. In the following section, the buoyancy effects on the rate of absorption in a rectangular enclosure is examined by comparing the results from diffusion and buoyancy-induced flow models. In the Analysis of heat transfer in a pipe section, simulation results of the heat transfer in a pipe are presented that allow the flow pattern in the DAR absorber to be predicted based on analogy. In the two sections following the analysis, mixed convection between parallel plates is investigated, and a range of parameters are varied to determine the effect of (1) the suction boundary condition; and (2) the Reynolds and Grashof numbers on absorption rate. The parallel plate geometry was chosen for these studies, because it allowed for a relatively simple simulation program to be developed with several features that were not available in the CFD package used for the study in the Analysis section.

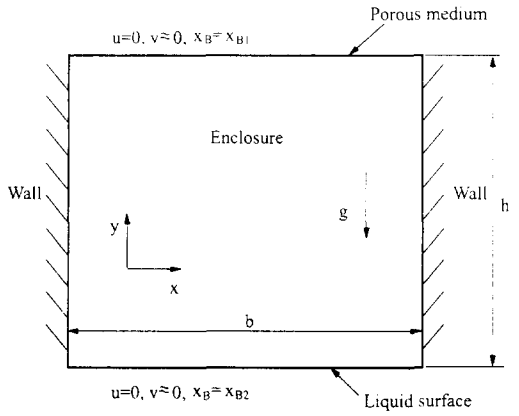

Figure 2 Absorption of a vapor in a square enclosure in the presence of a nonabsorbable vapor. The enclosure contains a binary vapor mixture (*A*, *B*). Density of *A* is much greater than the density of *B*. *B* is nonabsorbable at the bottom boundary $x_{B1} < x_{B2}$

Rectangular enclosure

The significance of the buoyancy effects on the rate of absorption in the absence of a forced flow can be clearly demonstrated by the following example. Consider a rectangular enclosure, as shown in Figure 2. A binary vapor mixture with components *A* and *B* is contained in the enclosure. Component *B* is assumed to be nonabsorbable in the liquid mixture containing components *A* and *C* at the bottom boundary, and component *C* is assumed to be nonvolatile. This situation is roughly analogous to the ammonia (*A*)–water(*C*)–hydrogen(*B*) system of interest in the present study. The two side walls are impermeable, and the top boundary is maintained at constant mass fraction x_{B1}. To simplify the problem further, the mass fraction of component *B* in the vapor phase at the bottom boundary is assumed to be constant at x_{B2} ($x_{B1} < x_{B2}$), and the process is assumed to be isothermal.

If components *A* and *B* have the same density, the only driving force would be mass diffusion. That is, component *A* would diffuse from the top to the bottom, and component *B* would be stagnant, because *B* is nonabsorbable at the interface. If the effect of the side walls on the velocity profile is neglected, a diffusion model is suitable (Bird et al. 1960) resulting in

$$n_{Ay}(\text{interface}) = \frac{\rho D}{h} \ln\left(\frac{x_{B1}}{x_{B2}}\right) \tag{2}$$

where n_{Ay} is the absolute mass flux of component *A* in the *y* direction, *D* is the binary mass diffusivity, *h* is the height of the enclosure, and ρ is the mixture density. Define a mass transfer coefficient h_m and Sherwood number (Sh) so that

$$n_{Ay}(\text{interface}) = \rho h_m (x_{B2} - x_{B1}) \tag{3}$$

$$\text{Sh} = \frac{h h_m}{D} \tag{4}$$

Table 1 Absorber inlet and outlet conditions

	Vapor outlet		Vapor inlet		Average mass concentration, kg/m³
	Mass fraction of NH_3	Density, kg/m³	Mass fraction of NH_3	Density, kg/m³	
Vapor (bulk)	0.221	2.48	0.626	4.36	1.64
Interface vapor	0.0842	2.16	0.367	2.87	0.618

Combining Equations 2–4 yields the following:

$$\mathrm{Sh} = \frac{\ln\left(\frac{x_{B2}}{x_{B1}}\right)}{(x_{B2} - x_{B1})} \tag{5}$$

Thus, the Sherwood number is the reciprocal of the log–mean mass fraction difference between the top and the bottom boundaries. That is $\mathrm{Sh} = \mathrm{Sh}(x_{B1}, x_{B2})$.

On the other hand, suppose that the density of component B is much less than component A. Because x_{B2} is greater than x_{B1}, the vapor mixture at the bottom (liquid–vapor interface) is lighter than the vapor mixture at the top. This density gradient tends to induce convection inside the enclosure due to buoyancy force.

An analogous heat transfer problem in a rectangular enclosure with a cold wall at the top, a hot wall at the bottom, and two side walls insulated was experimentally investigated by Globe and Dropkin (1959). They suggested the following heat transfer correlation

$$\mathrm{Nu} = 0.069\ \mathrm{Ra}^{\frac{1}{3}}\ \mathrm{Pr}^{0.074}$$
$$3E5 < \mathrm{Ra} < 7E9, \qquad 0.02 < \mathrm{Pr} < 8750 \tag{6}$$

This correlation has been confirmed by researchers and is given in several textbooks (Incropera and DeWitt 1990; Gebhart et al. 1988).

If the viscous dissipation, thermal-diffusion (Sorét) and diffusion-thermo (Dufour) effects are neglected, the energy and species transport equations take the same form. Then, if appropriate boundary conditions are used, Equation 6 can be interpreted as a mass transfer solution by analogy. Because the boundary condition at the interface for the heat transfer problem is given by

$$q_y(\text{interface}) = -k\left(\frac{\partial T}{\partial y}\right)_{\text{interface}} \tag{7}$$

and the boundary condition for the mass transfer problem is given by

$$n_{A_y}(\text{interface}) = -\frac{D}{x_{B2}}\left(\frac{\partial \rho_A}{\partial y}\right)_{\text{interface}} \tag{8}$$

The resulting mass transfer correlation can be written as

$$\mathrm{Sh} = 0.069\frac{1}{x_{B2}}\mathrm{Ra}_m^{\frac{1}{3}}\mathrm{Sc}^{0.074}$$
$$3E5 < \mathrm{Ra}_m < 7E9, \qquad 0.02 < \mathrm{Sc} < 8750 \tag{9}$$

The Sherwood numbers from the diffusion model (Equation 5) and the buoyancy-induced flow model (Equation 9) are plotted *versus* x_{B2} in Figure 3. It can be seen from the figure that the Sherwood numbers follow the same trend for both Equations 5 and 9. Because for the three solid curves, x_{B1} can be any positive number as long as it is smaller than x_{B2}, any one of these three solid curves can be compared with any one of the three dotted curves. If the highest solid curve is compared with the lowest dotted curve at $x_{B2} = 0.5$, the Sherwood number increases by a factor of 8.9 because of buoyancy effects. As Ra_m increases, the buoyancy effects increase. Equation 9 was applied to hydrogen and helium using experimental data ($\mathrm{Sc} = 0.957$, 1.01, and $\mathrm{Ra}_m = 2.04 \times 10^6$, 1.58×10^6 for hydrogen and helium, respectively from Kim et al. 1994). It was found that the Sherwood number for hydrogen was 9% greater than that for helium for this buoyancy-induced convection configuration. The enhancement of mass transfer rate is primarily attributable to the buoyancy-induced convection, which affects the distribution of mass fraction in the flow field and, thus, facilities the mass transfer process.

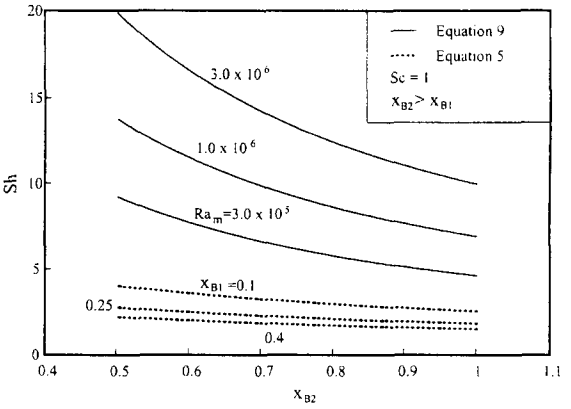

Figure 3 Sherwood number *versus* mass fraction of nonabsorbable gas B at the liquid–vapor interface

This analysis shows that buoyancy has a significant impact on mass transfer in an enclosure. However, the absorber problem of interest involves mixed convection in a tube. This geometry is modeled in the next section.

Analysis of heat transfer in a pipe

The absorption process posed in Figure 1 is a coupled heat and mass transfer problem involving both the liquid and vapor phases (Grossman 1983). In this section, the vapor side mass transfer process is modeled by analogy to a heat transfer problem. The following assumptions justify this approach.

(1) Buoyancy effects attributable to temperature can be neglected, because during the absorption process, the vapor side Grashof number Gr ($0 \sim 10^4$) is two orders of magnitude smaller than the mass transfer Grashof number Gr_m ($0 \sim 10^6$).
(2) The absorber of the DAR consists of 16 straight pipe sections connected by U-bends. For each section, the change of the liquid ammonia mass fraction is only approximately 1% on average. It is, therefore, reasonable to set a constant liquid mass fraction along a section, which eliminates the need to model the liquid side.
(3) The vapor is an ideal gas mixture.

Table 2 Heat transfer in a pipe solved using software fluent

Pipe geometry	$(r, z) = (0.05, 1)$ m, $\theta = 7°$
Mesh size	$(I, J, K) = (9, 17, 25)$, symmetrical meshes about y–z plane
Body force	$g_x = 0$, $g_y = -9.734$ m/s^2, $g_z = -1.195$ m/s^2
Boundary conditions	w (inlet) = 0.0275 m/s, T (inlet) = 273 K, $(u, v, w)_{\text{wall}} = (0, 0, 0)$
	$T_{\text{wall}}(-32° < \phi < 32) = 314.4$ K, T_{wall} (elsewhere) are insulated
Dimensionless no.	$\mathrm{Re} = 200$, $\mathrm{Gr} = 7.82 \times 10^6$, $\mathrm{Pr} = 0.717$
Convergence criteria	RES $(T, p, u, v, w) < 1 \times 10^{-5}$
Result	T_{avg}(outlet) = 300.03 K

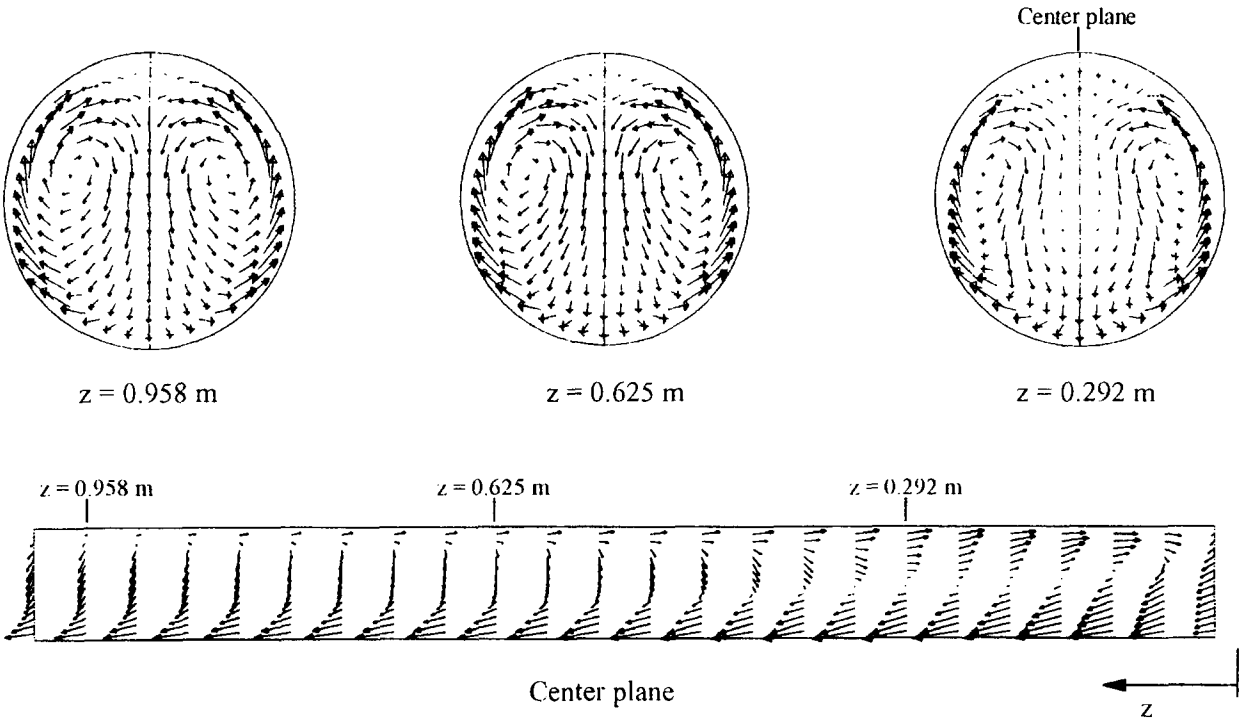

Figure 4 Velocity distributions in a pipe heated at the bottom (with buoyancy effects)

Assumptions 1 and 2 allow an uncoupled mass transfer model to be used to solve the vapor side buoyancy effects on the mass transfer. Then, assuming an analogy between the energy equation and species transport equation, a heat transfer model can be constructed to simulate the buoyancy effects in the absorption process.

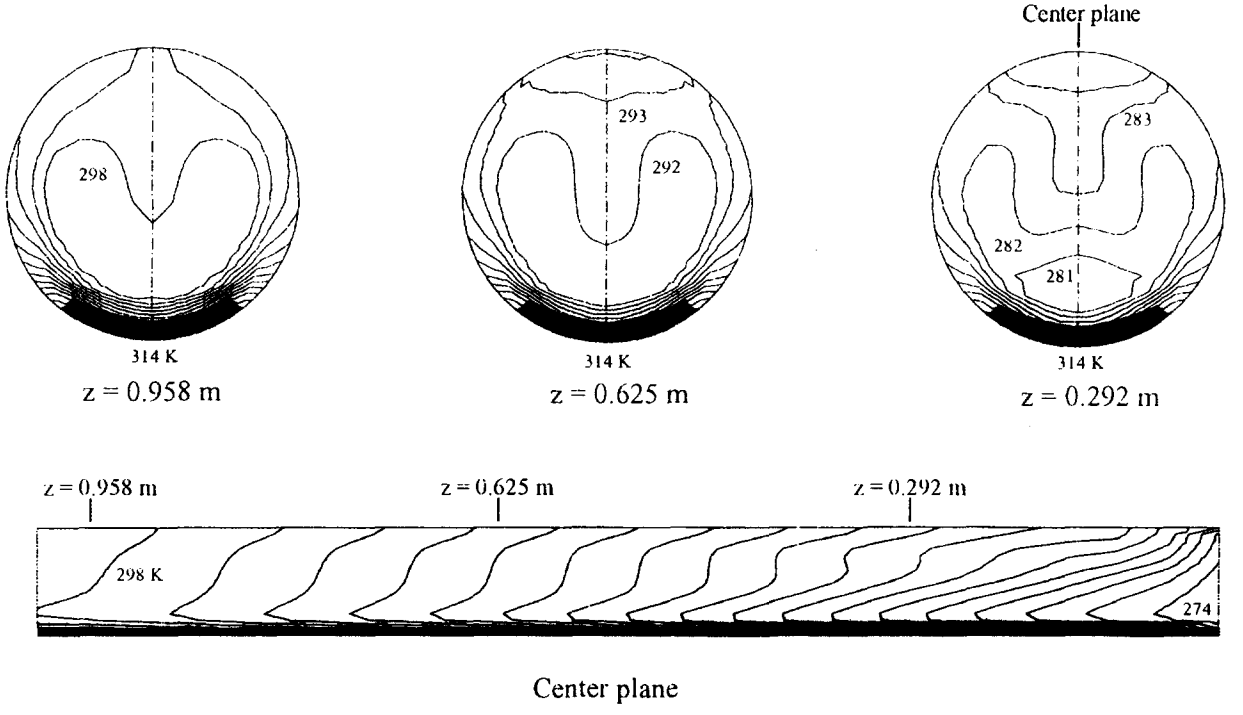

Re=200, Pr=0.717, Gr=7.8E6, ϕ=64°, θ=7°

Figure 5 Isotherms in a pipe heated at the bottom (with buoyancy effects)

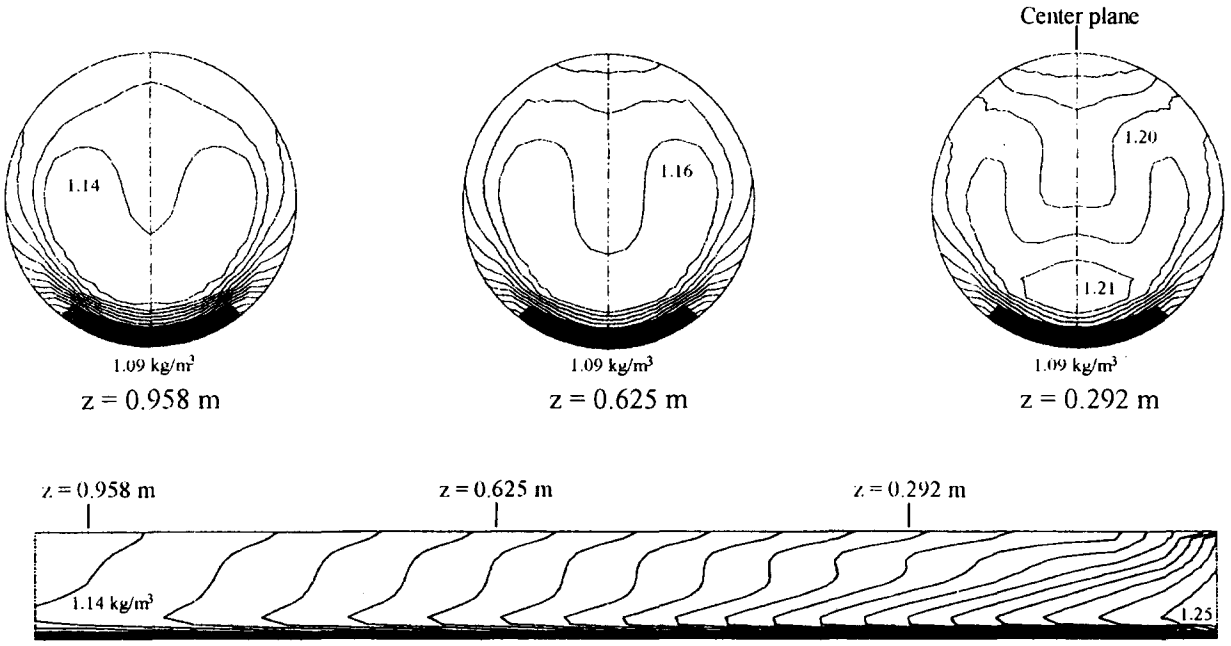

Re=200, Pr=0.717, Gr=7.8E6, ϕ=64°, θ=7°

Figure 6 Isochores in a pipe heated at the bottom (with buoyancy effects)

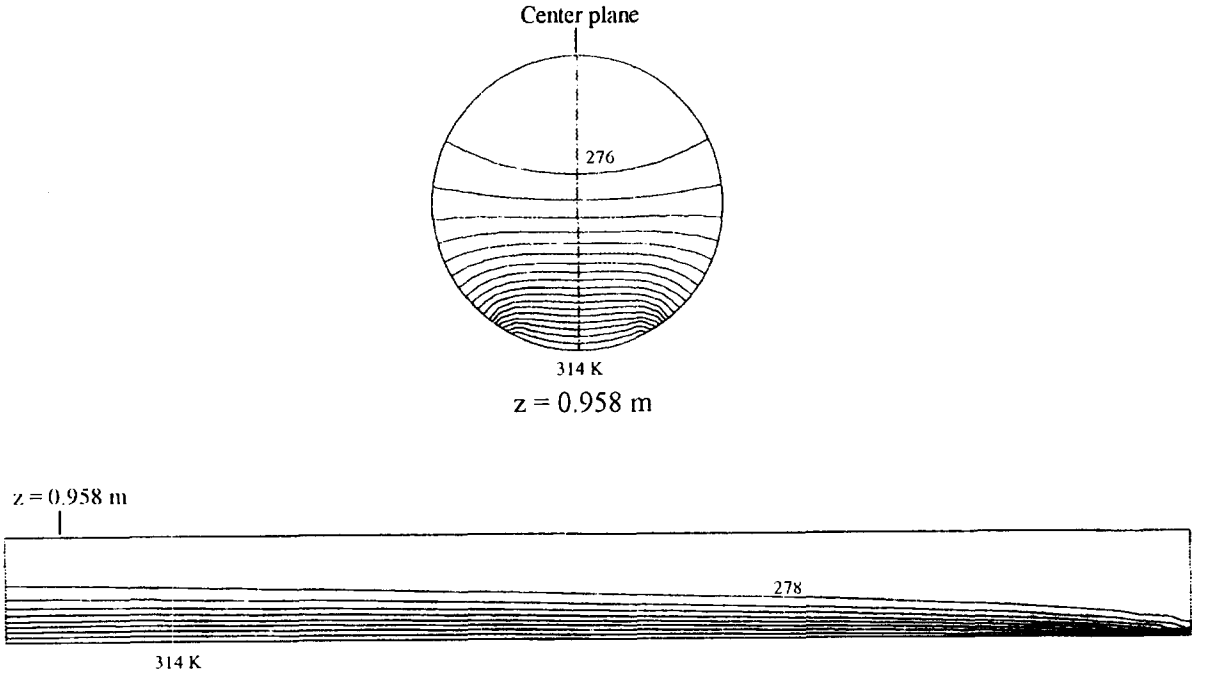

Re=200, Pr=0.717, Gr=0, ϕ=64°, θ=7°

Figure 7 Isotherms in a pipe heated at the bottom (without buoyancy effects)

The heat transfer in a circular pipe based on the above assumptions was solved using the software "Fluent" (Fluent 1994). Table 2 specifies the problem solved.

Figures 4, 5, and 6 show the velocity, temperature, and density distributions at three cross-section locations ($z = 0.292$, 0.625, and 0.958 m) with $z = 0$ on the left as well as a longitudinal cross section on the center plane. As shown in Figure 4, in each cross section, the cold fluid flows down along the centerline. The fluid gains heat from the bottom wall and flows up near the side walls. This cross-section flow pattern is superimposed on the forced main flow to form a helical circulation. In Figures 5 and 6, the values of isotherms and isochores are equally spaced. In Figure 5, the temperature at the center of three cross sections is lower than that of the two sides indicating that the cross-section flow facilitates the heat transfer process. As shown in Figure 6, the density and temperature (Figure 5) distributions resemble each other. This is attributable to the fact that the density is directly proportional to the temperature for an ideal gas model.

To demonstrate the buoyancy effects, a similar heat transfer problem was solved with the body force set to zero. Figure 7 shows the temperature distributions at a cross section near the outlet ($z = 0.958$ m), and in the longitudinal cross section. The average outlet temperature was found to be 281.17 K. That is, when buoyancy effects are present, the heat transfer is enhanced by a factor of 3.3.

For the DAR absorption process, the Gr_m, Re, and Sc are the same order of magnitude as the Gr, Re, and Pr mentioned above, respectively ($Gr_m = 1 \times 10^6 - 1 \times 10^7$, Re = 150 − 350, and Sc $\simeq 1$). By applying the heat and mass transfer analogy, a similar flow pattern is expected in the DAR absorber. In each cross section, the ammonia–hydrogen (or helium) mixture flows down near the center of the pipe. Because of the absorption of ammonia into the liquid absorbent film, the vapor mixture becomes lighter and flows up near the side walls. This cross-section flow pattern is superimposed on the forced main flow to form a helical circulation. In the DAR absorber, the buoyancy-induced convection is driven by composition changes, which change the density. This flow pattern facilitates the mass transfer on the vapor side and enhances the absorption process.

In the DAR absorber, the Gr_m for the ammonia–hydrogen vapor mixture is 29% greater than that of the ammonia–helium mixture. Therefore, the absorption rate from the ammonia–hydrogen mixture is expected to be greater than that from the ammonia–helium mixture.

Introduction to mixed convection mass transfer between parallel plates

In the previous sections, heat transfer models were used to investigate the mass transfer problem by analogy. That approach ignores the effect of the absorbed mass on the other field variables and, thus, is accurate only for low flux configurations. In this section, a 2-D version of the problem is solved, which accounts for the mass transfer fully. The approach is to solve a mixed convection mass transfer model between two parallel plates. The mass transfer (Sherwood number) dependence on the Gr_m and Re as well as the effects of suction boundary conditions are evaluated using the finite difference method.

Figure 8 gives a schematic diagram of the parallel plate geometry. A forced stream of binary mixture flows between two slightly inclined parallel plates. The absorbable component of the mixture (A) is absorbed into an absorbent liquid film containing components A and C flowing down the bottom plate. The length of the plates is extended beyond the absorption length (b/2) to allow an outflow boundary where diffusion can be neglected during the simulation.

The primary assumptions made to formulate the problem are: (1) 2-D, laminar, steady state; (2) Boussinesq approximation; (3) negligible Soret effects, (4) negligible buoyancy effects due to temperature gradient; (5) fully developed inlet velocity profile; (6) constant vapor mass fraction at the liquid–vapor interface; (7) negligible x-direction gradient in velocities and mass fraction at

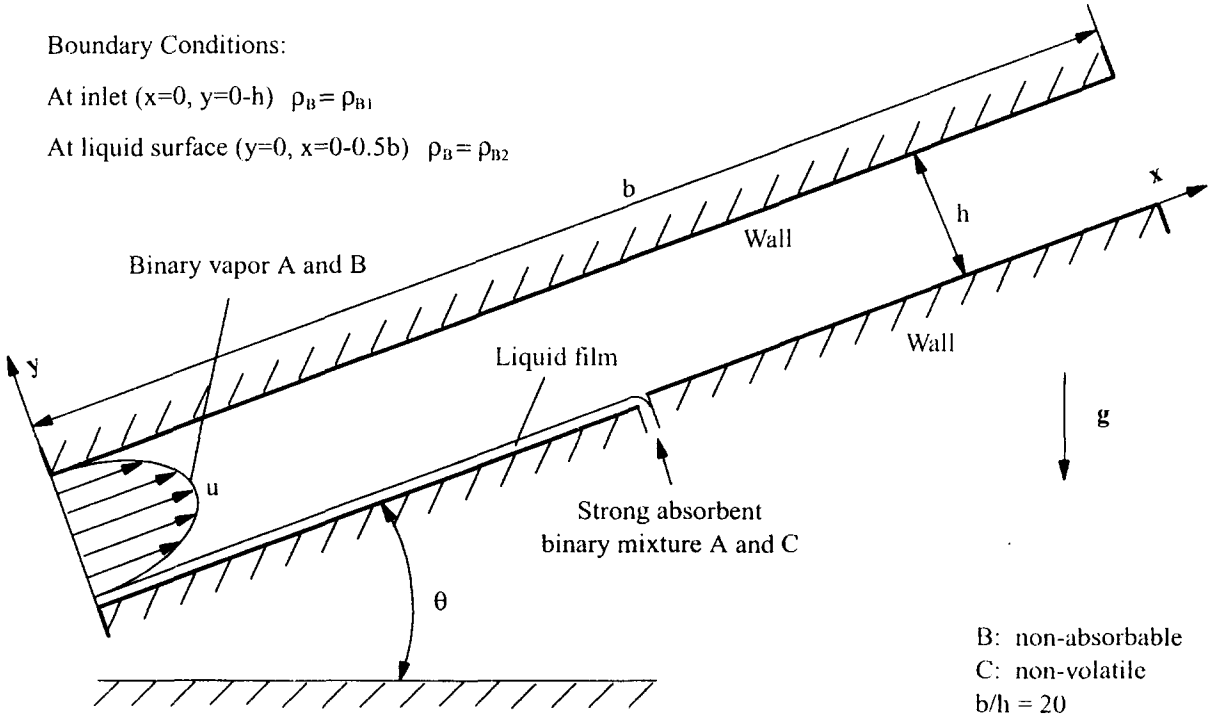

Figure 8 Absorption of binary mixture between two parallel plates

the vapor outlet; and (8) zero velocity at the liquid–vapor interface (a separate numerical study indicated that the Sherwood number variations attributable to shear from nonzero liquid velocity at the interface is less than 2.5% within the range of liquid mass flow rates in the DAR).

Under the above assumptions, the nondimensional equations governing the conservation of mass, momentum, species are, respectively

$$\frac{\partial U}{\partial X}+\frac{\partial V}{\partial Y}=0 \tag{10}$$

$$U\frac{\partial U}{\partial X}+V\frac{\partial U}{\partial Y}=-\frac{\partial P}{\partial X}+\frac{1}{\sqrt{\mathrm{Gr}_m}}\left(\frac{\partial^2 U}{\partial X^2}+\frac{\partial^2 U}{\partial Y^2}\right)+X_B\sin\theta \tag{11}$$

$$U\frac{\partial V}{\partial X}+V\frac{\partial V}{\partial Y}=-\frac{\partial P}{\partial Y}+\frac{1}{\sqrt{\mathrm{Gr}_m}}\left(\frac{\partial^2 V}{\partial X^2}+\frac{\partial^2 V}{\partial Y^2}\right)+X_B\cos\theta \tag{12}$$

$$U\frac{\partial X_B}{\partial X}+V\frac{\partial X_B}{\partial Y}=\frac{1}{\mathrm{SC}\sqrt{\mathrm{Gr}_m}}\left(\frac{\partial^2 X_B}{\partial X^2}+\frac{\partial^2 X_B}{\partial Y^2}\right) \tag{13}$$

where following scales are used

$$u_c=\sqrt{g\zeta h(\rho_{B2}-\rho_{B1})}\qquad U=\frac{u}{u_c}\qquad V=\frac{v}{u_c} \tag{14}$$

$$X=\frac{x}{h}\qquad Y=\frac{y}{h} \tag{15}$$

$$X_B=\frac{x_B-x_{B1}}{x_{B2}-x_{B1}} \tag{16}$$

$$P=\frac{p}{\rho u_c^2} \tag{17}$$

In the above equations, h is the distance between the two plates, and the species expansion coefficient ζ is defined as follows:

$$\zeta=-\frac{1}{\rho}\left(\frac{\partial\rho}{\partial\rho_B}\right)_{p,T} \tag{18}$$

The boundary conditions are posed as follows:

1. At the vapor inlet:

$$U(0,Y)=6\frac{\mathrm{Re}}{\sqrt{\mathrm{Gr}_m}}(Y-Y^2),\qquad V(0,Y)=0 \tag{19}$$

$$X_B(0,Y)=0 \tag{20}$$

2. At liquid-vapor interface:

$$V(0-10;0)=\left(1-\frac{x_{B1}}{x_{B2}}\right)\left(\frac{1}{\mathrm{Sc}\sqrt{\mathrm{Gr}_m}}\right)\left.\frac{\partial X_B}{\partial Y}\right|_{(0-10,0)} \tag{21}$$

$$U(0-10,0)=0,\qquad X_B(0-10,0)=0 \tag{22}$$

Equations 21 gives the dimensionless mass average velocity at the liquid–vapor interface base on a diffusion boundary condition. Because component A is absorbed (sucked) into the liquid, this boundary condition is referred to as a suction boundary condition in the remainder of this work. Here, $X_{B1}=\rho_{B1}/\rho$ and $X_{B2}=\rho_{B2}/\rho$ are constants representing mass fraction of component B at the vapor inlet and liquid–vapor interface, respectively. Note that the partial derivative in Equation 21 is coupled to the solution of Equations 10–13 and is not known a priori.

3. At the vapor outlet:

$$\left.\frac{\partial U}{\partial X}\right|_{(20,Y)}=\left.\frac{\partial V}{\partial X}\right|_{(20,Y)}=\left.\frac{\partial X_B}{\partial X}\right|_{(20,Y)}=0 \tag{23}$$

As shown in Figure 8, the parallel plates are extended beyond the absorption region. In this region, the velocity profile tends to be parabolic, and the mass fraction tends to be uniform, which

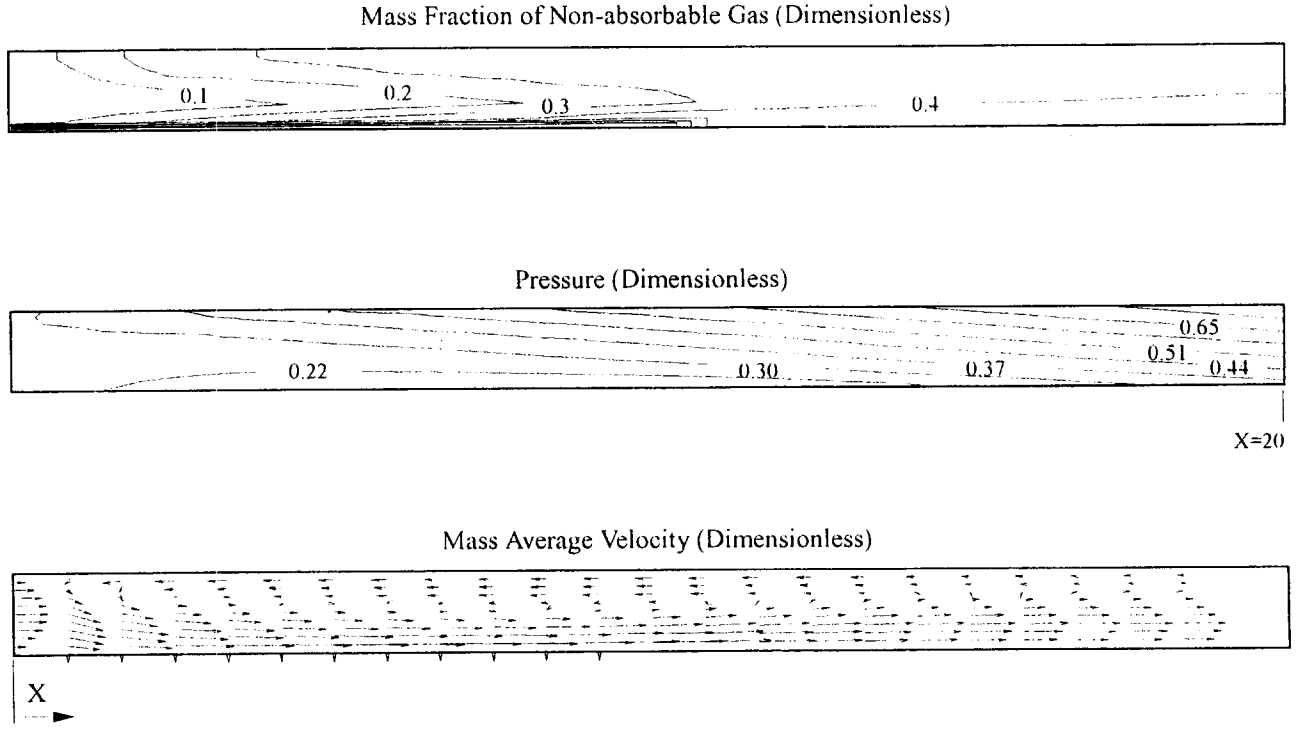

Figure 9 Mass fraction, pressure, and mass average velocity distributions; (Re = 200, Sc = 1, Gr_{in} = 4E6)

satisfies Equations 23. Even if the extended length is not long enough to allow Equations 23 to be satisfied exactly in the real situation, it allows the absorption rate half plate length away from the outlet to be evaluated with reasonable accuracy. During the present study, the dimensionless extended length was varied from 10 to 14. It was found that the solution in the absorption region was not sensitive to changes in this length. Therefore, the extended length was set to 10 during the parametric study.

4. At all other boundaries:

$$U(10-20, 0) = V(10-20, 0) = 0 \tag{24}$$

$$\left.\frac{\partial X_B}{\partial Y}\right|_{(10-20,0)} = 0 \tag{25}$$

$$U(10-20, 0) = V(10-20, 0) = 0 \tag{26}$$

$$\left.\frac{\partial X_B}{\partial Y}\right|_{(10-20,0)} = 0 \tag{27}$$

The governing equations (Equations 10–13) were solved numerically using a finite difference method with a staggered grid (Shih 1984). The dependent boundary condition (Equation 21) was incorporated by iteration. To validate and check the accuracy of the computer program, the heat transfer coefficient for a thermally fully developed flow between two parallel plates with constant wall temperatures was evaluated numerically. Compared to the analytical solution ($h_T = 3.77$), the calculated heat transfer coefficients were 3.65 for the mesh size (I, J) = (24, 12), and 3.76 for (I, J) = (40, 20). For the mass transfer calculations, the mesh size used was (I, J) = (40, 20).

Discussion of results

Referring to Figure 1, computations were performed for $\theta = 3°$, Pr = 1, Re = 50, 100, 200, and $Gr_m = 0 - 4 \times 10^6$. These parameters were chosen, because they are within the range encountered in the DAR absorption process. The dimensionless concentration gradient at the liquid–vapor interface (Sherwood number) was evaluated using the definition in Equation 4, and the mass transfer coefficient h_m is defined as follows:

$$h_m = \frac{\dfrac{D}{x_{B2}}\left.\dfrac{\partial x_B}{\partial y}\right|_{y=0}}{(x_{Bm} - x_{B2})} \tag{28}$$

where x_{Bm} is the mean mass fraction of the vapor mixture at a given cross section defined by

$$x_{Am} = \frac{\int_0^h u x_B \, dy}{\int_0^h u \, dy} \tag{29}$$

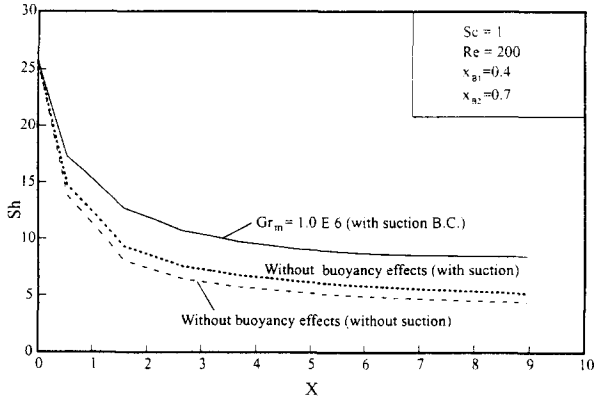

Figure 10 Sherwood number *versus* dimensionless distance from inlet

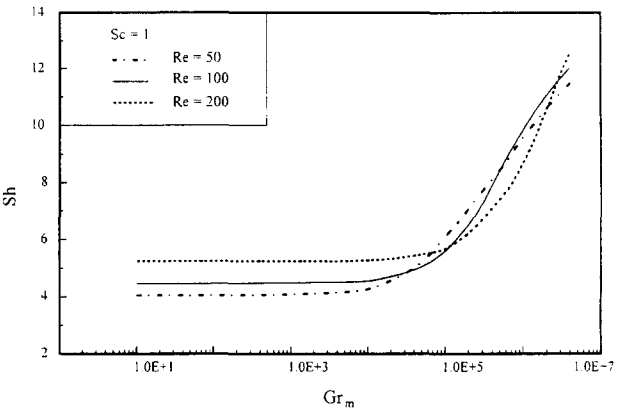

Figure 11 Sherwood number *versus* mass transfer Grashof number

The Sherwood number without the suction boundary conditions was also evaluated to quantify its effects on the mass transfer.

Figure 9 shows the distributions of mass fraction (nonabsorbable gas), pressure, and mass average velocity for Re = 200, $Gr_m = 4 \times 10^6$. As expected, the mass average velocity distribution resembles the center plane velocity distribution shown for the circular pipe case (Figure 4). A recirculation cell was generated by the buoyancy force. The magnitude of the X-directed velocity near the bottom plate where absorption occurs is significantly larger than that of the fully developed profile. The deformation of the velocity profile primarily due to buoyancy effects provides the mechanism of the mass transfer enhancement.

Figure 10 shows the Sherwood number *versus* dimensionless distance from the vapor inlet for conditions representative of the DAR absorber. Compared with the case without buoyancy effects and suction boundary conditions, the Sherwood number at $X = 9$ for $Gr_m = 1 \times 10^6$ increased by a factor of 2. Another factor worth noting is that the suction boundary condition has a measurable effect on the Sh, although it is not as important as the buoyancy effects.

In Figure 11, Sh at $X = 9$ is plotted *versus* Gr_m for Re = 50, 100, and 200. Sh at $X = 9$ is considered a representative value, because it is not changing significantly with X at this location for Re = 200 (see Figure 10) and is expected to be a representative value for other Re plotted in Figure 11 (Re < 200). As can be seen from Figure 11, the curves with different Re cross over for the following reasons.

(1) For small Gr_m($Gr_m = 10$), the otherwise constant Sh varies with Re because of the effects of the suction boundary condition. That is, the larger the Re, the greater the Sh when the buoyancy effects are negligible [Sh(Re = 50) = 4.025, Sh(Re-100) = 4.47, and Sh(Re = 200) = 5.23]. This is in contrast to the Nusselt number Nu for the same geometry, which is independent on Re. This result is dependent on the suction boundary condition, which represents a zero mass transfer resistance external to the computed region.

(2) The importance of buoyancy in mixed convection is measured by $Gr_m Re^2$. The greater this number, the greater the buoyancy effects (Incropera and DeWitt 1990). The buoyancy effects on the rate of absorption are mainly attributable to changes in the velocity field that facilitate the mixing of the interface vapor and the bulk vapor. The greater the Re, the greater the Gr_m required to alter the forced velocity field. Therefore, as Gr_m increases, Sh starts to increase earlier for the curve with Re = 50.

(3) From (1) and (2), it can be concluded that the three curves in Figure 11 have to cross over for the first time.

(4) The curves plotted in Figure 11 account for both the effects

of buoyancy and suction boundary condition. It is expected that for very large Gr_m, Sh for Re = 200 should be greater than that for Re = 50. This is because the greater the Re, the greater the effect of suction boundary condition on the Sh. Therefore, the curves in Figure 11 have to cross over for the second time.

For all the cases plotted in Figure 11, the Sherwood number (at $X = 9$) enhancement factor attributable to buoyancy effects is less than 3. The average Sherwood number over the absorption length is expected to have less enhancement, because the buoyancy effects are less important in the entrance region (see Figure 10).

According to Figure 11, Sh for the ammonia–hydrogen mixture increased by 11.3% compared to the ammonia–helium mixture using DAR test results ($Ra_m = 2.04 \times 10^6$, 1.58×10^6 for hydrogen and helium, respectively. Sc = 1, Re = 200 for both mixtures) (Kim et al. 1994). It should be mentioned that, in the DAR absorber, the Re for a hydrogen charge is greater than that for a helium charge with the same power input, and the geometry is different from the parallel plates. However, the result given here shows approximately how much the buoyancy effects can affect the absorption in the DAR.

Summary and conclusions

This study has elucidated the buoyancy effects on the mass transfer in absorption with nonabsorbable gas. Several assumptions have been made in the formulation. For example, the liquid side as well as the coupled heat transfer effects were not considered. However, based on our analysis the following conclusions can be made.

(1) The presence of a large density gradient attributable to mass fraction gradient results in significant mass transfer enhancement in absorption with a nonabsorbable gas. For the rectangular enclosure case, Sh for ammonia–hydrogen is 9% greater than that for ammonia–helium using DAR test results (Sc = 0.957, 1.01 and $Ra_m = 2.04 \times 10^6$, 1.58×10^6 for hydrogen and helium, respectively). For the parallel plates case, Sh for ammonia–hydrogen is 11.3% greater than that for ammonia–helium under similar conditions in the DAR absorber. For the circular pipe case, by applying the heat and mass transfer analogy, a helical circulation flow pattern is predicted in the DAR absorption process.

(2) The mechanism of the mass transfer enhancement is primarily due to the existence of buoyancy-induced flow, which facilitates the mixing of the bulk and interface fluids.

(3) Buoyancy effects gain importance at smaller Gr_m for smaller Re.

(4) The suction boundary condition makes a significant difference in the Sherwood number. When buoyancy effects are not present, Sh increases by approximately 11% as Re is doubled. The effect of suction boundary condition on mass transfer needs to be included to achieve accurate results.

References

Bird, R. B., Stewart, W. E. and Lightfoot, E. N. 1960. *Transport Phenomena*, Wiley, New York

Brauner, N. Maron, D. M. and Meyerson, H. 1989. Coupled heat condensation and mass absorption with comparable concentrations of absorbate and absorbent. *Int. J. Heat Mass Transfer*, **32**, 1897–1906

Burnett, J. C. and Himmelblau, D. M. 1970. The effect of surface active agents on interphase mass transfer. *AIChE J.*, **16**, 185–193

Cheng, K. C., Hong, S. W. and Hwang, G. J. 1972 Buoyancy effects on laminar heat transfer in the thermal entrance region of horizontal rectangular channels with uniform wall heat flux for large Prandtl number fluid. *Int. J. Heat Mass Transfer*, **15**, 1819–1836

Fluent. 1994. *Computational Fluid Dynamics Software*, Fluent, Inc., version 4.1

Gebhart, B., Yogesh, J., Roopl, L. M. and Bahgat, S. 1988. *Buoyancy-induced flows and transport*, Hemisphere Bristol, PA

Graetz, L. 1885. Üder die wärmeleitungsfahigket von flüssigkeiten. *Ann. Phys.*, **25**, 337–357

Grossman, G. 1983. Simultaneous heat and mass transfer in film absorption under laminar flow. *Int. J. Heat Mass Transfer*, **26**, 357–371

Grossman, G. 1990. Film absorption heat and mass transfer in the presence of non-condensables. *Proc. 9th Int. Heat Transfer Conference*, **6**, 247–252, Jerusalem, Israel

Grossman, G. 1991. The combined heat and mass transfer process in film absorption. *Proc. Absorption Heat Pump Conference*, 43–52

Kashiwagi, T. 1985. The activity of surfactant in high-performance absorber and absorption enhancement. *Refrigeration*, **60** 72

Kennedy, K. J. and Zebib, A. 1982. Combined force and free convection between parallel plates. *Proc. 7th Int. Heat Transfer Conference* 447–451, Munich, Germany

Kim, K. J., Chen, J., Shi, Z. and Herold, K. E. 1994. Diffusion-absorption heat pump. *Annual Report to Gas Research Institute*, GRI-94/0080

Mori, Y. and Futagami K. 1967. Forced convective heat transfer in uniformly heated horizontal tubes. *Int. J. Heat Mass Transfer*, **10**, 1801–1813

Ou, J. W., Cheng K. C. and Lin, R. C. 1974. Natural convection effects on Graetz problem in horizontal rectangular channels with uniform wall temperature of large Pr. *Int. J. Heat Mass Transfer*, **17**, 835–843

Patankar, S. V., Ramadhyani, S. and Sparrow, E. M. 1978. *J. Heat Transfer*, **100**, 63

Rashidi, M. Hetaroni G. and Banerjee, S. 1975. Mechanisms of heat and mass transport at gas–liquid interfaces, *Int. J. Heat Mass Transfer*, **18**, 901–910

Shi, Z. 1994. Performance modeling of the diffusion-absorption heat pump, *Master's thesis*, Department of Mechanical Engineering, University of Maryland, College Park, MD, USA

Shih, T. M. 1984. *Numerical Heat Transfer*. Hemisphere, Bristol, PA

Yih, S. M. and Seagrave, R. C. 1980. Mass transfer in laminar falling liquid film with accompanying heat transfer and interfacial shear. *Int. J. Heat Mass Transfer*, **23**, 749–758